EDGE ARTICLE

Check for updates

AI-enabled new sensing technology: colorimetric analysis of exosomes for precise diagnosis of breast cancer

Xinyu Qu,[a] Bingqian Lu,[a] Chengge Gao,[a] Weizun Zhao,[b] Yujing Zeng,[c] Shuai Wu,*[d] Chenbo Ji [ID] *[efg] and Genxi Li [ID] *[ac]

Colorimetric sensors are widely utilized in biomedical detection owing to their simple operation and intuitive visual results. However, their inherent limitation in the output signal makes sensors insufficient in handling multiple biomarker combination information required for the diagnosis of highly heterogeneous diseases like breast cancer. To overcome the limitation, this study draws inspiration from the mechanism by which the human visual system perceives a myriad of colors using only three cone cell types. So, we propose a novel AI-enabled bionic mixed-color sensing technology for accurate breast cancer subtyping through exosome (EXO) analysis. This technology gives EXO a unique "mixed color fingerprint" by simultaneously binding color-coded nanoprobes (Ab-DyeNPs) targeting different proteins (PD-L1, EpCAM, and HER-2) on the EXO. This mixed-color signal is subsequently recognized by computer vision and analyzed using machine learning algorithms to yield a diagnostic conclusion. For cell line models, this technology accurately differentiates various breast cancer subtypes, reaching up to 100% accuracy. More importantly, it achieved 96.7% accuracy in subtyping clinical samples, outperforming both single-target and multi-target analysis strategies. This study transforms complex multi-dimensional biological information into intuitive visual data, providing a rapid and highly accurate novel tool for precise subtyping of breast cancer, which holds significant potential for clinical application.

1. Introduction

Colorimetric sensors, a classic biosensing technology, have become an essential tool in biomedical detection due to their significant advantages, including simple operation, low cost, and intuitive visual results.[1–4] For instance, to diagnose breast cancer, colorimetric sensing strategies have been successfully applied for the non-invasive screening of specific biomarkers, such as human epidermal growth factor receptor-2 (HER-2) and the estrogen receptor, providing essential references for clinical decision-

[a] State Key Laboratory of Analytical Chemistry for Life Science, School of Life Sciences, Nanjing University, Nanjing 210023, PR China

[b] Institute of AI for Industries, Nanjing 211135, PR China

[c] Center for Molecular Recognition and Biosensing, School of Life Sciences, Shanghai University, Shanghai 200444, PR China

[d] Clinical Medicine Research Institute, The First Affiliated Hospital with Nanjing Medical University, Nanjing 210029, Jiangsu, PR China

[e] State Key Laboratory of Reproductive Medicine and Offspring Health, Nanjing Women and Children's Healthcare Institute, Women's Hospital of Nanjing Medical University, Nanjing Women and Children's Healthcare Hospital, Nanjing Medical University, Nanjing 210004, PR China

[f] Jiangsu Provincial Key Laboratory of Biological Therapy for Organ Failure, Nanjing Medical University, Nanjing 210004, PR China

[g] Nanjing Medical Key Laboratory of Female Fertility Preservation and Restoration, Nanjing 211166, PR China

making.[5–7] However, colorimetric sensors also have an inherent limitation: the output signal typically manifests as a single-dimensional color intensity change, such as 3,3′,5,5′-tetra-methylbenzidine molecules transitioning from colorless to deep blue[8,9] or shifts toward specific single hues, like gold nanoparticles changing from red to blue.[10,11] While this one-dimensional signal mode can achieve sensitive detection of single targets, it is difficult to synchronously analyze combinatorial information from multiple indicators in complex biological systems, severely limiting its application in high-order diagnostic scenarios that require multi-parameter synergistic interpretation.[12,13]

Interestingly, the human visual system exhibits excellent color perception,[14,15] yet this relies solely on the combinatorial encoding mechanism of three types of cones, each sensitive to a specific wavelength of red, green, and blue light (RGB), respectively.[16–18] The myriad colors in nature are essentially the result of the superposition and mixing of different proportions of the three primary colors of light.[19] This principle equally applies to coloration – the three primary colors of pigments (cyan, magenta, yellow, CMY) can theoretically be mixed in different proportions to create nearly infinite unique hues.[20] This fundamental principle from biomimetics and color science may offer crucial insight for overcoming the information bottleneck of the colorimetric sensor: encoding only a limited number of basic color elements can form composite color

outputs that cover a wide color gamut.[21,22] By designing sensing systems capable of generating multiple chromogenic reactions in parallel, it should be possible to encode and map concentration information from multiple independent analytes onto a composite, highly distinguishable, specific mixed-color "fingerprint". This "mixed-color" strategy should be able to expand single-dimensional intensity signals into high-dimensional chromaticity space, thereby significantly enhancing the information throughput of the colorimetric sensors and multi-target analytical capabilities.

The high heterogeneity of breast cancer is a typical example of such multi-target analytical requirements.[23] Breast cancer is not a single disease, but encompasses multiple molecular subtypes with significant differences, with each subtype exhibiting fundamental differences in pathological characteristics, therapeutic responses, and prognosis.[24,25] Accurate subtyping is the cornerstone for developing individualized precision treatment regimens, such as HER-2 targeted therapy for the HER-2 subtype.[26] Breast cancer exosomes (EXOs), as carriers of tumor information, are promising biomarkers of subtyping diagnosis.[27] In addition to the increased content of breast cancer EXO in patients' body fluids, it is worth noting that breast cancer EXO presents specific proteins derived from the original tumor cells.[28,29] However, existing technologies for breast cancer EXO detection are limited primarily to single-target protein analysis (one-dimensional), such as CD63,[30] HER-2,[31] and EpCAM,[32] which cannot address the demand for precise identification and analysis of breast cancer EXO. Although some multiplexed detection techniques have been proposed,[33,34] they are mostly simple parallel arrangements of multiple independent one-dimensional detections, resulting in cumbersome operations, high sample consumption, time-consuming procedures, and high costs. This discrete analytical mode fails to meet clinical demands for rapid and integrated subtyping. If multi-dimensional information could be compressed into a single mixed-color signal for rapid analysis, it would greatly simplify the subtyping workflow.

So, inspired by the color recognition capabilities of the human visual system, this study addresses the challenges in breast cancer diagnosis by proposing a new sensing technology. The fabricated colorimetric sensor is based on mixed-color signals, combined with artificial intelligence (AI) for analysis, to achieve multidimensional data extraction and then precise breast cancer subtyping. Scheme 1 illustrates the principle of this sensor. First, nanoparticles encapsulating different dye molecules (DyeNPs) are synthesized through hydrophobic interactions and further functionalized with antibodies to confer targeting capabilities, thereby constructing color-encoded analysis probes (Ab-DyeNPs). Then, magnetic beads (MBs) modified with targeting phosphatidylserine (PS) peptides are employed for EXO isolation,[35] which can provide high capture efficiency while avoiding masking of target proteins. Subsequently, the Ab-DyeNPs respond synergistically to different proteins on the EXO, producing a specific mixed-color fingerprint code. Finally, the analysis of breast cancer subtypes is achieved by the sensor, which combines computer vision and machine learning algorithms. This strategy proposed in this work may break through the barriers to
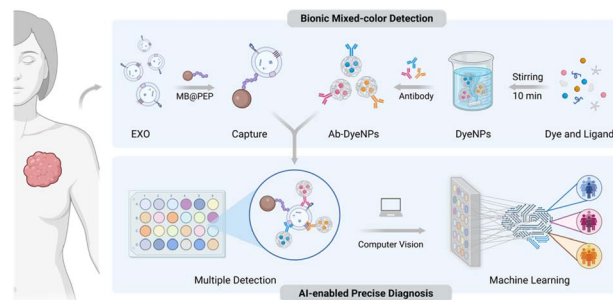
Scheme 1 Principles of AI-enabled colorimetric analysis of EXO for precise diagnosis of breast cancer.

monochromatic changes, extending the output dimension from one dimension to multiple dimensions, which can significantly improve information and discrimination capabilities. After combining with AI to identify and analyze the signals, the complex process of "color decoding" is transformed into an intuitive "diagnostic conclusion", enabling precise typing of breast cancer and supporting clinical practice.

2. Results and discussion

2.1. Characterization and performance of Ab-DyeNPs

As shown in Fig. 1A, based on the hydrophobic properties of pH-sensitive dyes, DyeNPs were synthesized by loading the three dye molecules, including thymolphthalein (TP), phenolphthalein (PP) and curcumin (CUR), through the hydrophobic pockets of bovine serum albumin (BSA).[36] The assembly time was significantly reduced to 10 min under the synergistic effects of polyethylene glycol (PEG) and tannic acid (TA). Among them, PEG can increase the local concentration of ligands, and TA not only has a strong hydrophobic effect to promote assembly but also further adsorbs antibodies.[37,38] DyeNPs were formed by adding TA to the pre-mixed solution of other ligands and dyes (Fig. S1). SEM images revealed that DyeNPs are uniform and monodisperse particles (Fig. 1B–D). Their sizes have been 277.7 ± 17.2 nm (TPNPs), 301.4 ± 18.7 nm (PPNPs), and 293.5 ± 18.1 nm (CURNPs), respectively (Fig. 1E–G). Monitoring the size of DyeNPs using different dispersants revealed that DyeNPs were unaffected in water, 100 mM NaCl (electrostatic competitor), and 100 mM urea (hydrogen bond competitor), but were effectively disassembled in Tween 20, primarily due to the disruption of hydrophobic interactions (Fig. S2A and B). Significantly, the dye loading capacities achieved by DyeNPs—73.13% (TP), 68.11% (PP), and 67.87% (CUR)—are markedly higher than those reported for comparable materials. Examples include mesoporous silica nanoparticles (1.9%)[39] and the metal–polydopamine framework (41.2%).[40]

Functionalization of DyeNPs was verified using Cy3-labeled antibodies. Fluorescence imaging of DyeNPs (Fig. S3A) and Cy3-Ab-DyeNPs (Fig. S3B) was conducted, with the latter exhibiting distinct fluorescent signals, confirming the successful immobilization of the antibody. It is well established that pH indicator dyes undergo structural changes accompanied by distinct color variations through rapid proton exchange in the presence of OH^- ions (Fig. 1H–J).[41,42] To verify that pH indicator
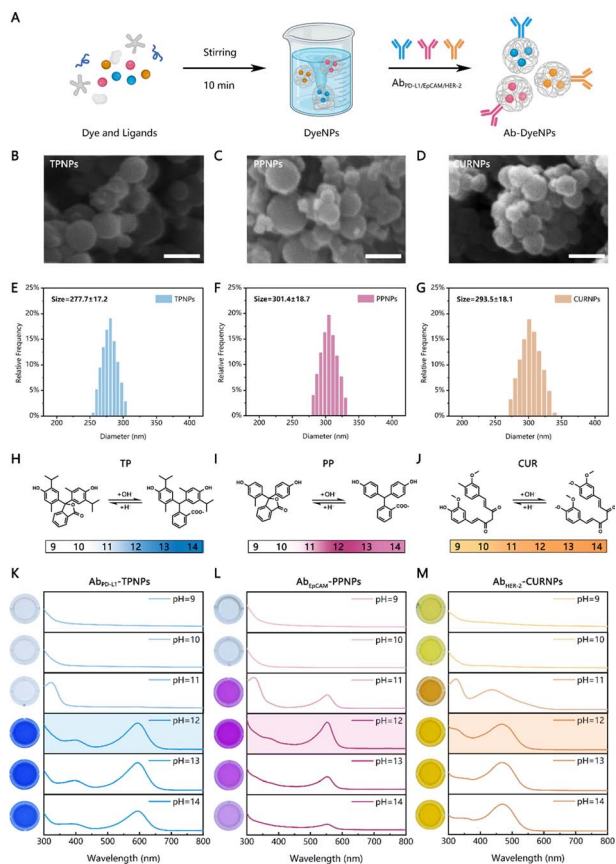
Fig. 1 (A) Schematic diagram of the Ab–DyeNP synthesis method. SEM image of (B) TPNPs, (C) PPNPs, and (D) CURNPs. Scale bars, 500 nm. DLS results of (E) TPNPs, (F) PPNPs, and (G) CURNPs. Chromogenic mechanism of (H) TP, (I) PP, and (J) CUR. The absorbance values of the (K) Ab_{PD-L1}-TPNPs, (L) Ab_{EpCAM}-PPNPs, and (M) Ab_{HER-2}-CURNPs at varying pH values.

molecules can be released from Ab-DyeNPs and induce color changes in alkaline solutions, we incubated Ab-DyeNPs with chromogenic solutions of varying pH values (pH 9.0–14.0). To obtain maximum colorimetric signals for subsequent sensor array applications, we ultimately selected pH = 12 for subsequent experiments (Fig. 1K–M). Furthermore, to construct a stable sensor platform, we evaluated the temperature tolerance and storage stability of Ab-DyeNPs. The results demonstrated that the absorbance values of Ab-DyeNPs (Fig. S4A–C) remained stable across a wide temperature range, exhibiting superior sensor potential compared to horseradish peroxidase, whose activity declined sharply with increasing temperature (Fig. S5). Additionally, Ab-DyeNPs maintained excellent chromogenic capability after 7 days of storage (Fig. S6). Based on these findings, the system demonstrates not only rapid response capability for colorimetric detection but also reliable performance under diverse environmental conditions.

2.2. Construction and optimization of single-color detection module

To specifically identify biomarkers on EXO, we first successfully isolated EXO from the culture media of MDA-MB-231, MCF-7,

and SK-BR-3 cells. The typical cup-shaped structures of the three types of EXO could be observed in TEM images, and nanoparticle tracking analysis (NTA) further revealed the hydrodynamic diameter of the EXO (Fig. 2A–C). Isolating EXO under complex biological fluid conditions is the basis for accurate analysis. PS is known to be exosome-specific,[43,44] and its unique location can provide a good immunoaffinity-related strategy. Furthermore, tumor-derived EXO overexpressed PS in their adventitial leaflets compared with normal cellular EXO.[45] Therefore, we can isolate tumor EXO by targeting the lipid layer with MB functionalized with PS-targeting peptides (MB@PEP), and avoid shielding biomarkers on EXO to be tested. To characterize their capture, DiO-prestained EXOs were incubated with MB@PEP, and intense green fluorescence was observed around MB@PEP. In contrast, no fluorescence was observed around the naked MB, serving as a control (Fig. 2D), which demonstrates successful capture.

Subsequently, we utilized the magnetic beads with captured EXO to trigger the sensor further and validate its feasibility. As shown in Fig. S8, all three probes could detect their corresponding targets with relatively independent maximum absorption peaks. The analytical results for all three membrane proteins showed significant color differences compared to the blank control (Fig. 2E), proving the feasibility of EXO analysis. To improve biosensor performance, we optimized various experimental parameters, including the concentration of modifying peptides, the capture time of EXO using magnetic beads, the probe incubation time, and the working concentrations of the
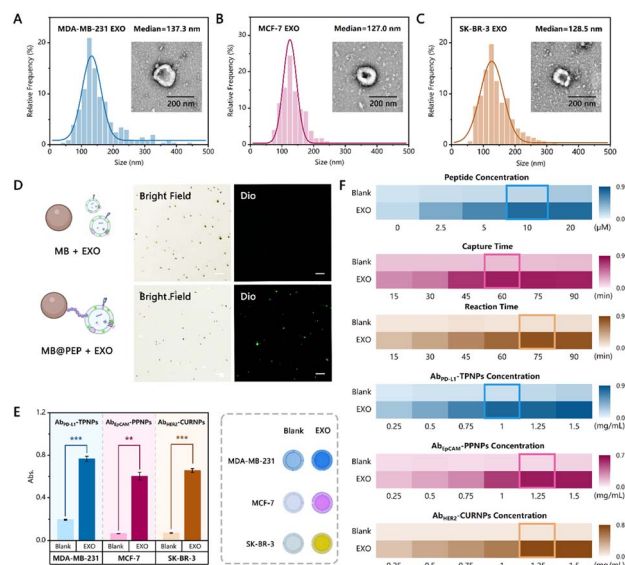

Fig. 2 Nanoparticle tracking analysis of normal EXO derived from (A) MDA-MB-231, (B) MCF-7, and (C) SK-BR-3 cells. Inset: TEM image of EXO isolated from the culture media of MDA-MB-231, MCF-7, and SK-BR-3 cells. (D) Fluorescence microscopy images of MB and MB@PEP with DiO-stained EXO. Scale bars, 10 μm. (E) Results of this colorimetric biosensor for target detection, including the measurement of the UV-vis absorption spectrum, and the corresponding visualization results. (F) Optimization of experimental parameters: the concentration of modifying peptides, the capture time of EXO using magnetic beads, the probe incubation time, and the working concentrations of the three probes.

three probes (Fig. 2F). The optimal experimental parameters were determined by comparing signal-to-noise ratios and visualization efficiency. Finally, we selected a peptide concentration of 10 μM (Fig. S9), a capture time of 60 min (Fig. S10), an incubation time of 75 min (Fig. S11), and probe working concentrations of 1 mg mL^{-1}, 1.25 mg mL^{-1}, and 1.25 mg mL^{-1} (Fig. S12–S14), respectively, for subsequent analyses.

2.3. Performance of the single-color detection module

We first evaluated the single-target quantitative detection capability of the biosensor by detecting EXO from MDA-MB-231, MCF-7, and SK-BR-3 cells using Ab$_{PD-L1}$-TPNPs, Ab$_{EpCAM}$-PPNPs, and Ab$_{HER-2}$-CURNPs, respectively. The results demonstrated that the absorbance of all three probes exhibited a positive correlation with EXO concentration (Fig. 3A–C). This linear relationship was attributed to the fact that a greater number of EXOs can bind more signal probes, thereby releasing more chromogenic dyes in the presence of OH^{-}. As shown in Fig. 3D–F, the absorbance displayed a linear relationship with the logarithm of EXO concentration, with a detection limit of 10^3 particles per mL, which is superior to existing methods (Table S1). Subsequently, we conducted specificity validation using targeted free proteins and a standard breast epithelial cell line (MCF-10A) as control groups (Fig. S15). The results indicated that only groups containing corresponding EXO produced intense color changes, demonstrating the sensor's excellent selectivity. To further evaluate the detection performance of our method in complex environments, we tested the colorimetric signals of different EXO concentrations in 10% FBS. As illustrated in Fig. S16, the signal values in PBS and 10% FBS were approximately equivalent, indicating that this method possesses outstanding anti-interference capability in complex biological matrices.

2.4. EXO analysis of breast cancer cell lines by bionic mixed-color visual sensing technology

Encouraged by the good detection effect of monochrome modules, we expanded this method to mixed-color encoding detection and output the detection results with computer-aided
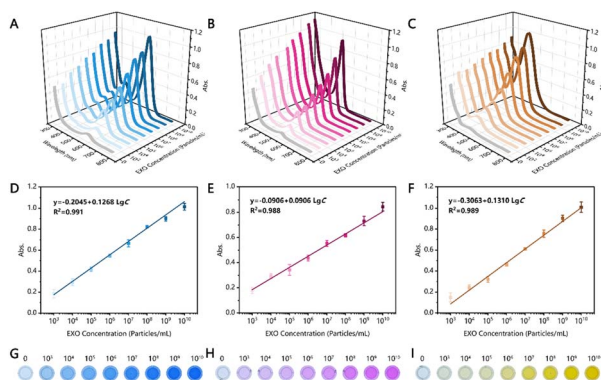
decoding (Fig. 4A). The breast cancer cell lines MDA-MB-231, SK-BR-3, and MCF-7 exhibit distinct molecular profiles and have been widely used to model different breast cancer subtypes. We utilized our constructed sensor to perform surface protein analysis of EXO from these different subtypes, using EXO derived from the healthy breast cell line MCF-10A as a control. As observed, MDA-MB-231, SK-BR-3, and MCF-7 EXO expressed varying levels of PD-L1, EpCAM, and HER-2 on their membranes (Fig. 4B). Specifically, our method determined that the expression levels of all three proteins in the control group (MCF-10A) were significantly lower than in the other groups. For SK-BR-3, a classic model for HER-2-positive breast cancer (HER-2$^+$), the expression level of HER-2 was substantially higher than that of other subtypes. MDA-MB-231, a model for the most aggressive triple-negative breast cancer subtype (TNBC), also showed a relatively abundant expression of PD-L1. The expression levels of exosomal PD-L1, EpCAM, and HER-2 highlight the distinct profiles and differential expression of these biomarkers on various types of EXOs (Fig. 4C). These findings were largely consistent with the western blot results (Fig. S17). Therefore, specific detection and classification of these EXOs can be achieved by quantifying the surface levels of PD-L1, HER-2, and EpCAM.

Subsequently, we established a computer vision-based system for multiplexed co-detection to perform subtyping analysis of EXO from these breast cancer cell lines, with the specific workflow detailed in Fig. 4D. The sample images are automatically positioned and identified using computer vision
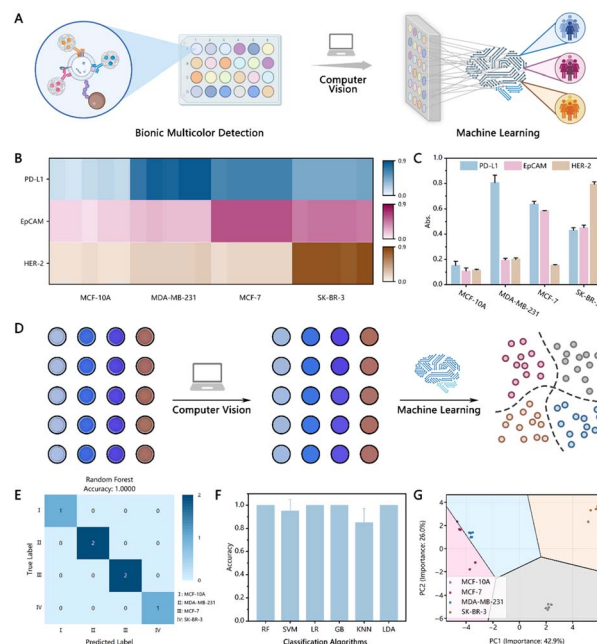

Fig. 4 (A) Specific process diagram of bionic mixed-color visual sensing technology. (B) Heatmap of expression of PD-L1, EpCAM, and HER-2 proteins on EXO. (C) Target protein levels on different breast cancer cell lines (MCF-10A, MCF-7, MDA-MB-231, and SK-BR-3). (D) Computer vision-based machine learning color classifier. (E) Confusion matrix for the random forest classifier's performance across breast cancer cell lines. (F) Comparative performance evaluation of different machine learning classifiers. (G) Linear classifier decision boundaries in principal component space for classification.

Fig. 3 UV-vis absorption spectra of (A) MDA-MB-231, (B) MCF-7, and (C) SK-BR-3 EXO with different concentrations. A linear relationship between the UV-vis absorption peak value and the concentration of (D) MDA-MB-231, (E) MCF-7, and (F) SK-BR-3 EXO. The visualization detection result of (G) MDA-MB-231, (H) MCF-7, and (I) SK-BR-3 EXO.

(Fig. S18). To minimize systematic errors from single-point sampling, we employed an average pixel value extraction algorithm to quantify color features. Following this, six representative classifiers were selected to apply for pattern recognition and classification of the four EXO subpopulations, as they cover diverse learning paradigms including ensemble, distance-based, linear, and kernel-based approaches (Table S3), namely K-Nearest Neighbors (KNN), Random Forest (RF), Gradient Boosting (GB), Linear Discriminant Analysis (LDA), Logistic Regression (LR), and Support Vector Machine (SVM). The test set confusion matrices (Fig. 4E and S19) show that all six algorithms performed well in EXO subtyping. Cross-validation results indicated that the accuracy of RF, GB, and LR methods reached 100% (Fig. 4F). The mixed-color features of EXO demonstrated significant differences and excellent diagnostic performance in distinguishing subtypes, effectively discriminating between the single-subtype EXO (Fig. 4G). These results suggest that this computer vision-based biosensor holds significant potential for breast cancer subtyping analysis.

2.5. Clinical sample validation

Encouraged by the promising results from the cell line-based subtype analysis, we proceeded to perform subtype analysis of clinical samples. We selected serum samples from healthy individuals ($n = 20$), HER-2$^+$ patients ($n = 20$), and TNBC patients ($n = 20$) for sensor evaluation (Table S2). The heatmap illustrates the abundance of the three membrane proteins in EXO from each subject in the training cohort (Fig. 5A). Notably, each protein exhibited a high degree of heterogeneity among patients of different subtypes. Despite differences in protein expression levels, the distribution between the two groups still showed considerable overlap, both in the breast cancer diagnosis and subtype analysis (Fig. 5B and S20). Even with the integration of machine learning algorithms, the accuracy of single-target analysis was insufficient for clinical application, and multi-target analysis also presented certain limitations (Fig. 5C and S21).

Our computer vision biosensor is used to detect and analyze clinical samples, converting visual information into quantitative color-feature data through automated image recognition technology (Fig. 5D). A comparative performance analysis revealed that the image recognition-based method demonstrated significantly superior performance in the subtyping task compared to both single-target and multi-target analysis strategies (Fig. 5E and S22). This advantage likely stems from the ability of image data to provide richer and more comprehensive sample features than absorbance values at a single wavelength. Subsequently, cross-validation was used to systematically evaluate the six machine learning algorithms to obtain performance metrics including accuracy, recall, precision, F1-score, and loss (Fig. 5F and S23). Due to its inherent limitations in handling high-dimensional color features based on the linear separability assumption, LDA performed poorly in the complex color pattern recognition task, resulting in relatively low classification accuracy (Fig. S24). In contrast, the RF algorithm excelled in this task with a cross-validation accuracy of up to 96.7%, primarily due to its ensemble learning architecture and strong adaptability to
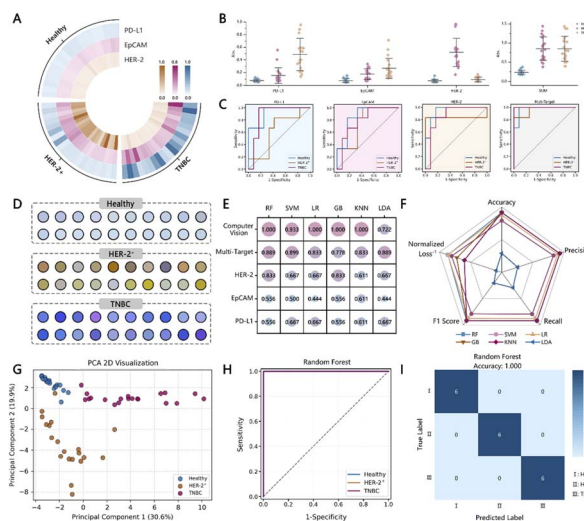

Fig. 5 (A) Heatmap of expression levels of PD-L1, EpCAM, and HER-2 proteins on EXO in clinical samples. (B) Scatter plot of expression levels of PD-L1, EpCAM, HER-2 proteins, and SUM (PD-L1 + EpCAM + HER-2) on EXO in clinical samples. (C) ROC curves for single-target and multi-target classification. (D) Computer vision-processed images of clinical samples after automated identification. (E) Comparative classification performance of different classifiers across computer vision, multi-target, and single-target approaches. (F) Cross-validation performance radar chart for different classifiers applied to clinical samples using computer vision-based classification. (G) PCA visualization of clinical sample data points after dimensionality reduction, grouped by sample category. (H) ROC curves for the random forest classifier performance on clinical sample classification. (I) Confusion matrix for random forest identification of clinical samples.

nonlinear relationships. By constructing multiple decision trees and employing an ensemble voting mechanism, RF effectively captures complex patterns and non-linear trends within the mixed-color data (Fig. 5G). The algorithm's robust generalization ability for color gradients and continuous feature variations enabled it to achieve optimal classification precision in the EXO subtype colorimetric recognition task, successfully subtyping the clinical samples of the test set with an accuracy of up to 100% (Fig. 5H and I). Therefore, this computer vision-based biosensor holds excellent potential for the clinical analysis of breast cancer subtypes, serving as a valuable tool to aid in physician diagnosis.

3. Conclusion

This study has developed a novel AI-enabled colorimetric sensing technology that successfully addresses the limitations of conventional colorimetric methods in the synchronous analysis of multiple indicators. This technology transforms complex molecular recognition events into an information-rich and intuitive high-dimensional hybrid color by designing multicolor-encoded nanoprobes targeting multiple key proteins on the EXO. Subsequently, a computer vision system captures this unique visual signal, which is then deeply analyzed and precisely classified by machine learning algorithms, particularly the high-performing RF model, to achieve the precise identification of breast cancer subtypes. This fabricated sensor performs excellently in terms of specificity, sensitivity, and

stability, enabling the accurate typing of cell lines and clinical samples. The sensor also achieves a diagnostic accuracy of up to 96.7% in clinical sample tests, surpassing traditional analytical methods and demonstrating its strong potential for multi-component analysis. The method in the work, which encodes and compresses multidimensional biological information into visual "mixed-color" signals, may propose an entirely new model for colorimetric sensors, providing a promising new path for non-invasive, rapid, and precise typing of breast cancer and other complex diseases.

Ethics approval

The clinical samples of 20 HER-2$^+$ breast cancer patients, 20 TNBC breast cancer patients, and 20 voluntarily donated healthy individuals were obtained from the First Affiliated Hospital of Nanjing Medical University (the information of all the patients was summarized in Table S2). Prior approval was obtained from the ethics committees (Project Number: 2019-SRFA-139), and clinical experiments were conducted in accordance with ethical standards. Informed consents were obtained from human participants of this study.

Author contributions

Xinyu Qu: writing – original draft, methodology, investigation, conceptualization, funding acquisition. Bingqian Lu: methodology, investigation. Chengge Gao: methodology, formal analysis. Weizun Zhao: methodology, software. Yujing Zeng: validation, methodology. Shuai Wu: writing – review & editing, investigation, funding acquisition. Chenbo Ji: resources, supervision, investigation. Genxi Li: writing – review & editing, project administration, investigation, funding acquisition.

Conflicts of interest

There are no conflicts to declare.

Data availability

The data that support the findings of this study are available from the corresponding author upon reasonable request.

Supplementary information (SI) is available. See DOI: https://doi.org/10.1039/d5sc06650f.

Acknowledgements

Notes and references

1 Z. Jin, W. Yim, M. Retout, E. Housel, W. Zhong, J. Zhou, M. S. Strano and J. V. Jokerst, *Chem. Soc. Rev.*, 2024, **53**, 7681–7741.

2 F. Mazur, Z. Han, A. D. Tjandra and R. Chandrawati, *Adv. Mater.*, 2024, **36**, e2404274.

3 S. H. Nah, J. B. Kim, H. N. T. Chui, Y. Suh and S. Yang, *Adv. Mater.*, 2024, **36**, e2409297.

4 R. Liu, J. Li, B. J. Salena and Y. Li, *Angew. Chem., Int. Ed.*, 2025, **64**, e202418725.

5 R. Kim, B. Mun, S. Lim, C. Park, J. Kim, J. Lim, H. Jeong, H. Y. Son, H. W. Rho, E. K. Lim and S. Haam, *Small*, 2024, **20**, e2307262.

6 Q. Liang, Q. Zhou, H. Shi, S. Wu, J. Yang, T. Zeng, J. Zhao, Y. Yin and G. Li, *Nano Today*, 2024, **54**, 102143.

7 W. Cheng, Y. Yao, D. Li, C. Duan, Z. Wang and Y. Xiang, *Biosens. Bioelectron.*, 2023, **238**, 115552.

8 Y. Ren, L. Cao, H. Li, R. Jiao, Y. Zhan, X. Zhang, X. Yu, M. Li, W. Wu, Z. Liang, G. Li, X. Xia, D. Zhang, N. Ling and Y. Ye, *ACS Nano*, 2025, **19**, 23703–23718.

9 J. Xu, G. Weng, J. Li, J. Yang, J. Zhu and J. Zhao, *Chem. Eng. J.*, 2025, **513**, 162799.

10 T. Yang, Z. Luo, Y. Tian, C. Qian and Y. Duan, *TrAC, Trends Anal. Chem.*, 2020, **124**, 115795.

11 W. Liu, A. Soliman, H. E. Emam, J. Zhang, J. V. Bonventre, L. P. Lee and M. L. Nasr, *ACS Nano*, 2025, **19**, 17514–17524.

12 R. Deng, K. Zhang, L. Wang, X. Ren, Y. Sun and J. Li, *Chem*, 2018, **4**, 1373–1386.

13 T. Zhai, Q. Li, J. Shen, J. Li and C. Fan, *Aggregate*, 2020, **1**, 107–116.

14 J. L. Schnapf, T. W. Kraft and D. A. Baylor, *Nature*, 1987, **325**, 439–441.

15 S. Thorpe, D. Fize and C. Marlot, *Nature*, 1996, **381**, 520–522.

16 T. D. Lamb, *Eye*, 2016, **30**, 179–185.

17 J. K. Bowmaker and D. M. Hunt, *Curr. Biol.*, 2006, **16**, R484–R489.

18 D. Mustafi, A. H. Engel and K. Palczewski, *Prog. Retinal Eye Res.*, 2009, **28**, 289–302.

19 B. Wandell and L. D. Silverstein, *The Science of Color*, 2003, pp. 281–316.

20 Y. Zhang, Y. Yu and J. Y. Ying, *Adv. Funct. Mater.*, 2022, **32**, 2109553.

21 D. Mao, X. Tang, R. Zhang, T. Chen, C. Liu, H. Gou, P. Sun, Y. Mao, J. Deng, W. Li, F. Sun and X. Zhu, *J. Am. Chem. Soc.*, 2024, **146**, 16428–16439.

22 D. Mao, X. Tang, R. Zhang, S. Hu, H. Gou, P. Zhang, W. Li, Q. Pan, B. Shen and X. Zhu, *Nat. Commun.*, 2025, **16**, 958.

23 X. Xiong, L. Zheng, Y. Ding, Y. Chen, Y. Cai, L. Wang, L. Huang, C. Liu, Z. Shao and K. Yu, *Signal Transduction Targeted Ther.*, 2025, **10**, 49.

24 S. Loibl, P. Poortmans, M. Morrow, C. Denkert and G. Curigliano, *Lancet*, 2021, **397**, 1750–1769.

25 C. A. Adebamowo, E. Ezeome, K. T. Yawe, O. Ayandipo, O. Badejo, S. N. Adebamowo, I. B. Achusi, A. Fowotade and G. O. Ogun, *J. Clin. Oncol.*, 2022, **40**, 548.

26 X. Zhang, Y. Gao, X. Zhang, N. Guo, W. Hou, S. Wang, Y. Zheng, N. Wang, H. Liu and B. Wang, *Pharmacol. Ther.*, 2023, **245**, 108417.

27 Y. Zhou, L. Tao, J. Qiu, J. Xu, X. Yang, Y. Zhang, X. Tian, X. Guan, X. Cen and Y. Zhao, *Signal Transduction Targeted Ther.*, 2024, **9**, 132.

28 M. A. Kumar, S. K. Baba, H. Q. Sadida, S. A. Marzooqi, J. Jerobin, F. H. Altemani, N. Algehainy, M. A. Alanazi, A. Abou-Samra, R. Kumar, A. S. Al-Shabeeb Akil, M. A. Macha, R. Mir and A. A. Bhat, *Signal Transduction Targeted Ther.*, 2024, **9**, 27.

29 Y. Cao, X. Yu, T. Zeng, Z. Fu, Y. Zhao, B. Nie, J. Zhao, Y. Yin and G. Li, *J. Am. Chem. Soc.*, 2022, **144**, 13475–13486.

30 X. Guan, J. Zhao, Z. Sha, Y. Liang, J. Huang, J. Zhang and S. Sun, *Biosens. Bioelectron.*, 2024, **259**, 116380.

31 R. Kim, B. Mun, S. Lim, C. Park, J. Kim, J. Lim, H. Jeong, H. Y. Son, H. W. Rho, E. K. Lim and S. Haam, *Small*, 2024, **20**, 2307262.

32 X. Meng, X. Zhao, W. Liu, Y. Wang, J. Chen, K. Chang and P. Chen, *Nano Today*, 2025, **65**, 102854.

33 X. Su, X. Liu, Y. Xie, M. Chen, C. Zheng, H. Zhong and M. Li, *ACS Nano*, 2023, **17**, 4077–4088.

34 X. Wang, J. Wang and S. Xu, *Chem. Eng. J.*, 2025, **506**, 159904.

35 Y. Chen, Y. Huang, Q. Li, Z. Luo, Z. Zhang, H. Huang, J. Sun, L. Zhang, R. Sun, D. J. Bain, J. F. Conway, B. Lu and S. Li, *Nat. Nanotechnol.*, 2023, **18**, 193–204.

36 W. Xu, L. Jiao, H. Ye, Z. Guo, Y. Wu, H. Yan, W. Gu, D. Du, Y. Lin and C. Zhu, *Biosens. Bioelectron.*, 2020, **148**, 111780.

37 B. Yu, Z. Xiao, S. Shao, M. Yang, H. Jing, S. Shen, Z. Cao and X. Yang, *Adv. Funct. Mater.*, 2025, **35**, 2417548.

38 B. You and C. Chen, *ACS Nano*, 2024, **18**, 33545–33554.

39 F. Shao, L. Zhang, L. Jiao, X. Wang, L. Miao, H. Li and F. Zhou, *Anal. Chem.*, 2018, **90**, 8673–8679.

40 R. Ren, G. Cai, Z. Yu, Y. Zeng and D. Tang, *Anal. Chem.*, 2018, **90**, 11099–11105.

41 X. Wang, S. Cheng, X. Wang, L. Wei, Q. Kong, M. Ye, X. Luo, J. Xu, C. Zhang and Y. Xian, *ACS Sens.*, 2021, **6**, 1925–1932.

42 L. Chen, Y. Li, L. Miao, X. Pang, T. Li, Y. Qian and H. Li, *Biosens. Bioelectron.*, 2021, **188**, 113308.

43 K. Yang, M. Jia, S. Cheddah, Z. Zhang, W. Wang, X. Li, Y. Wang and C. Yan, *Bioact. Mater.*, 2022, **15**, 343–354.

44 Y. Su, Q. Gao, R. Deng, L. Zeng, J. Guo, B. Ye, J. Yu and X. Guo, *Mater. Today Bio*, 2022, **16**, 100434.

45 Y. T. Kang, E. Purcell, C. Palacios Rolston, T. W. Lo, N. Ramnath, S. Jolly and S. Nagrath, *Small*, 2019, **15**, 1903600.